nature COMMUNICATIONS

ARTICLE

https://doi.org/10.1038/s41467-020-19511-4 OPEN

Spin-orbit torque switching of an antiferromagnetic metallic heterostructure

Samik DuttaGupta[1,2,3✉], A. Kurenkov[1,2,3], Oleg A. Tretiakov[4], G. Krishnaswamy[5], G. Sala[5], V. Krizakova[5], F. Maccherozzi[6], S. S. Dhesi[6], P. Gambardella[5], S. Fukami[1,2,3,7,8] & H. Ohno[1,2,3,7,8]

The ability to represent information using an antiferromagnetic material is attractive for future antiferromagnetic spintronic devices. Previous studies have focussed on the utilization of antiferromagnetic materials with biaxial magnetic anisotropy for electrical manipulation. A practical realization of these antiferromagnetic devices is limited by the requirement of material-specific constraints. Here, we demonstrate current-induced switching in a polycrystalline PtMn/Pt metallic heterostructure. A comparison of electrical transport measurements in PtMn with and without the Pt layer, corroborated by x-ray imaging, reveals reversible switching of the thermally-stable antiferromagnetic Néel vector by spin-orbit torques. The presented results demonstrate the potential of polycrystalline metals for antiferromagnetic spintronics.

[1] Center for Science and Innovation in Spintronics, Tohoku University, 2-1-1 Katahira, Aoba-ku, Sendai 980-8577, Japan. [2] Center for Spintronics Research Network, Tohoku University, 2-1-1 Katahira, Aoba-ku, Sendai 980-8577, Japan. [3] Laboratory for Nanoelectronics and Spintronics, Research Institute of Electrical Communication, Tohoku University, 2-1-1 Katahira, Aoba-ku, Sendai 980-8577, Japan. [4] School of Physics, The University of New South Wales, Sydney 2052, Australia. [5] Laboratory for Magnetism and Interface Physics, Department of Materials, ETH Zurich, 8093 Zurich, Switzerland. [6] Diamond Light Source, Chilton, Didcot, Oxfordshire OX11 0DE, United Kingdom. [7] Center for Innovative Integrated Electronic Systems, Tohoku University, 468-1 Aramaki Aza Aoba, Aoba-ku, Sendai 980-0845, Japan. [8] WPI Advanced Institute for Materials Research, Tohoku University, 2-1-1 Katahira, Aoba-ku, Sendai 980-8577, Japan. ✉email: sdg@riec.tohoku.ac.jp

The capability to utilize antiferromagnets (AFMs) as multifunctional components of spintronic devices has opened new avenues for future spintronic devices[1–13]. Previous works utilizing antiferromagnetic heterostructures have demonstrated promising characteristics suitable for AFM-based memories[7,8], AFM/ferromagnet (FM) spin-orbit torque (SOT) device for spintronics-based neuromorphic hardware[8,9], and skyrmion-based computing[11]. Realizing the full potential of antiferromagnetic spintronics requires AFM-based components that can complement the essential functions of existing FM-based spintronics devices. To achieve this objective, the capability to electrically record and retrieve information from an antiferromagnetic material is of paramount importance. Previous works investigated the interaction of current with the antiferromagnetic Néel vector (staggered moment) resulting in anisotropic and spin-Hall magnetoresistance (SMR) effects[14–17], which can serve as an electrical probe for reading. Switching of an AFM either by field-like Néel SOTs originating from inverse spin galvanic effects[7,18–21] or SOTs in AFM-insulator/heavy metal (HM) heterostructures[22–24] and electric field control of Néel SOTs[25] have been demonstrated, offering techniques to manipulate antiferromagnetic Néel vector. However, a practical realization of these antiferromagnetic devices relies on the requirement of materials obeying certain crystallographic or magnetic symmetries[7,18–21,26] and epitaxy of the AFM with adjacent layers of the heterostructures[22–24]. A second challenge constraining the choice of material systems for antiferromagnetic spintronics concerns the stability of recorded information. Antiferromagnetic materials possessing a high thermal stability factor (Δ) could be beneficial for robust storage of information free from thermally-activated intrinsic relaxation dynamics[20,27,28]. These requirements for reading, writing, and storage of information pose a stringent set of parameters limiting the materials available for antiferromagnetic spintronics. Mn-based binary metallic alloys (ex. PtMn, IrMn, etc.) corresponds to a class of specialized material, traditionally utilized in spin-valve structures owing to its capabilities of significant exchange bias field, low processing temperatures, and compatibility with Si-based electronics. The favorable combination of room temperature ordering[29,30], high thermal stability[31], significant bulk uniaxial magnetic anisotropy[32], and magnetoresistive effects in PtMn for reading[17] renders this material feasible for future antiferromagnetic spintronic devices.

Here, we show electrical writing of information in polycrystalline AFM/HM metallic structures. Electrical measurements supplemented by x-ray magnetic dichroism imaging show a deterministic reversal of the antiferromagnetic Néel vector in the metallic AFM PtMn. A comparison of electrical measurements of antiferromagnetic heterostructures with and without HM layer clarifies the underlying role played by SOTs in switching. We also demonstrate the capability of PtMn for long-time data retention due to a high thermal stability factor, intrinsic to this material[31]. The present experimental results demonstrate the prospect of metallic AFMs for future antiferromagnetic spintronic devices.

Sample fabrication and properties. The stack structures are deposited by magnetron sputtering on highly resistive Si substrates with a natural oxidation layer. We utilize sub./Ta(3)/Pt(3)/MgO(2)/$Pt_{0.38}Mn_{0.62}$($10 \le t_{PtMn} \le 30$)/Pt(5)/Ru(1) (PtMn(t_{PtMn})/Pt, hereafter), where the numbers in parentheses are the nominal thicknesses in nm ((Fig. 1(a))). The obtained results are compared to reference structure sub./Ta(3)/Pt(3)/MgO(2)/$Pt_{0.38}Mn_{0.62}$($10 \le t_{PtMn} \le 30$)/Ru(1) (PtMn(t_{PtMn})/Ru, hereafter). The deposited films are patterned into star-shaped structures by photolithography and Ar ion milling. After fabrication, we anneal the structures at 300 °C for 2 h. Out-of-plane x-ray diffraction (XRD) spectra indicate a textured polycrystalline orientation along the (111) direction (see supplementary Fig. S1), consistent with previous reports[31,33]. We obtain an average grain size of 10 ± 2 nm by using Scherrer's formula. Magnetization hysteresis loops (m-H loops) of annealed PtMn/Pt and PtMn/Ru blanket films show a small magnitude of areal magnetic moment (m) indicating the antiferromagnetic nature of the thin films (Fig. 1(b)). The finite m can possibly arise from minute fractions of disordered moments and/or inhomogeneous multi-domain antiferromagnetic configuration (shown later). Additional m–H measurements of annealed PtMn(10)/$[Co(0.3)/Ni(0.6)]_2$/Co(0.3)/MgO(2)/Ru(1) AFM/FM heterostructures show a shifted loop indicating the presence of exchange bias[3,34], which is further proof of antiferromagnetic ordering as shown in Fig. 1(b). The star-shaped patterned samples are characterized by electrical and optical measurements. Figure 1(c)–(f) schematically shows the sequence of electrical measurements. Electrical writing of information is achieved by sourcing pulsed currents ($I_{1,2}$) along two orthogonal directions (A(C)→B(D)) while the corresponding resistance state is read-out by measuring the transverse Hall resistance (R_{Hall}) of the sample using a dc current (I_{DC}) of much weaker amplitude than $I_{1,2}$[17]. A waiting time of 10 s is employed after each write pulse. The electrical switching measurements are supplemented by x-ray magnetic linear dichroism (XMLD) measurements performed by photoemission electron microscopy (PEEM) imaging on sub./Ta(3)/Pt(5)/$Pt_{0.38}Mn_{0.62}$(10)/Ru(1) structures (Pt/PtMn(10), hereafter) before and after the injection of current pulses. The position of the Pt layer in these stacks are reversed to enhance magnetic contrast from the PtMn layer. The combination of electrical measurements and XMLD-PEEM imaging enables us to clarify the characteristics of current-induced switching in the AFM PtMn.

Results

Experiments on current-induced switching of AFM/HM and AFM structures. First, we investigate the current-induced switching of AFM/HM structures under the application of current pulses of varying amplitude at a constant pulse width (τ_P).

Ten I_1 pulses are sourced along the horizontal arm (A→ B) followed by I_2 pulses along the vertical arm (C→ D). We measure R_{Hall} after each I_1 or I_2 pulse, enabling us to detect possible changes in Néel vector under the application of current. Figure 1g shows the results of PtMn(10)/Pt for different current amplitudes at a constant τ_P. The application of I_1 pulse results in a high-resistance state (red-rimmed circles in Fig. 1g) while I_2 pulse corresponds to a low-resistance state (blue-rimmed circles in Fig. 1g). This distinct nature of R_{Hall} persists for different applied pulse amplitudes irrespective of t_{PtMn} (see supplementary Fig. S2a, b), demonstrating the intrinsic nature of the observed behavior. Considering R_{Hall} as a measure of the averaged antiferromagnetic Néel vector, distinct reversal changes under I_1 and I_2 indicate a possibility of antiferromagnetic Néel vector switching or reorientation in our AFM/HM structure. To confirm the stability of the switched states, we monitor R_{Hall} for several hours after application of I_1 or I_2 (Fig. 1h). Clear, distinguishable resistive states without any sign of relaxation are observed, indicating high thermal stability of AFM PtMn[30]. Under a macrospin approximation, the thermal stability factor (Δ) of an antiferromagnetic grain is expressed as $\Delta = \frac{K_U V}{k_B T}$, where K_U is the anisotropy energy density, V is the grain volume, k_B is the Boltzmann constant and T is temperature. Assuming $K_U \approx 1.4 \times 10^6$ J m^{-3}, from previous works[32], and 10 nm grain size evaluated from XRD, we obtain $\Delta \ge 150$ at 300 K, significantly higher than most of previously studied antiferromagnetic materials (~40–60)[20–24,26,27].

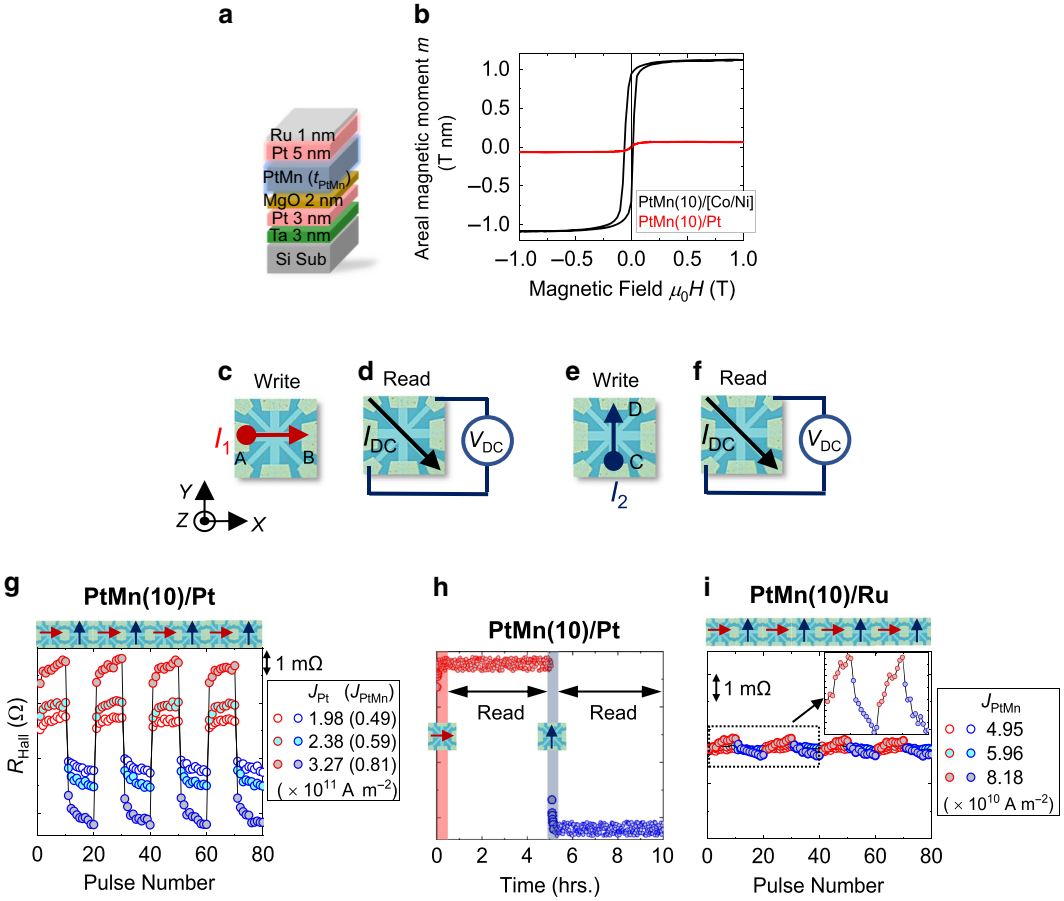

Fig. 1 Stack structure, schematics of measurement configuration, and current-induced switching. (**a**) Schematic diagram of the stack structure. (**b**) areal magnetic moment (m) vs magnetic field (H) for sub./PtMn(10)/[Co(0.3)/Ni(0.6)]$_2$/Co(0.3)/MgO(2)/Ru(1) (PtMn(10)/[Co/Ni]) and PtMn(10)/Pt structure. (**c**)-(**f**) Optical micrograph of the star-shaped device structure and schematic diagram of the measurement set-up. Write currents I_1 and I_2 are sourced along the paths from A(C) to B(D), respectively. Reading of the antiferromagnetic states is achieved by measuring transverse Hall voltage (V_{DC}) under the application of read current (I_{DC}) along the arm aligned at 45° to the write channel. (**g**) Experimental results of current-induced manipulation of PtMn(10)/Pt structure under applied current densities $J_{Pt} = 1.98 \times 10^{11}$ A m^{-2} ($J_{PtMn} = 4.96 \times 10^{10}$ A m^{-2}) $J_{Pt} = 2.38 \times 10^{11}$ A m^{-2} ($J_{PtMn} = 5.95 \times 10^{10}$ A m^{-2}) and $J_{Pt} = 3.27 \times 10^{11}$ A m^{-2} ($J_{PtMn} = 8.17 \times 10^{10}$ A m^{-2}). (**h**) The stability of written states was investigated by measuring R_{Hall} for several hours after writing. Red and blue shaded area corresponds to the writing of PtMn(10)/Pt by 10 write pulses along a direction indicated by the arrows in the schematics. The scale bar of the y-axis (R_{Hall}) is same as of (**g**). (**i**) Results of current-induced manipulation of PtMn(10)/Ru structure under applied $J_{PtMn} = 4.95 \times 10^{10}$, 5.96×10^{10}, and 8.18×10^{10} A m^{-2} respectively. Inset shows a magnified view of R_{Hall} vs pulse number characteristics for $J_{PtMn} = 8.18 \times 10^{10}$ A m^{-2} for the area bounded by the rectangular box. Schematic diagrams above (**g**) and (**i**) denotes the sequence of application of I_1 and I_2 in the respective structures.

Owing to the metallic nature of these structures, applied $I_{1,2}$ results in current flowing through both AFM and HM layers. This charge current in the HM or AFM can separately result in charge-to-spin conversion effects[35–39], both of which are capable of current-induced switching of antiferromagnetic Néel vector. To disentangle these contributions, we compare the experimental results for PtMn(10)/Pt with similar measurements on PtMn(10)/Ru at identical device dimensions (Fig. 1i). The write current density in PtMn (J_{PtMn}) is kept similar to that in PtMn(10)/Pt enabling a direct comparison between these two structures. As opposed to distinct reversible R_{Hall} states in PtMn(10)/Pt, we observe a gradual change of R_{Hall} in PtMn(10)/Ru, whose magnitude is smaller by a factor of 10 (inset of Fig. 1i). We also compare the results on PtMn(10)/Pt with similar experiments on sub./Ta(3)/Pt(5)/Ru(1) structures (see Supplementary Fig. S3a, b). No significant changes in R_{Hall} are observed at comparable current densities for this structure and PtMn/Pt, ruling out any sizeable contribution from anisotropic thermoelectric effects towards the observed R_{Hall} behavior[40].

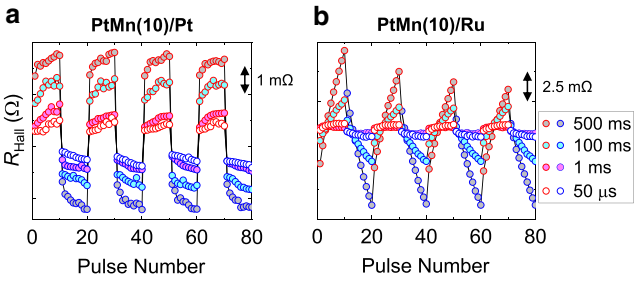

Fig. 2 Different characteristics of current-induced switching between PtMn/Pt and PtMn/Ru structures. (**a**) Pulse width (τ_P) dependence of transverse Hall resistance (R_{Hall}) for PtMn(10)/Pt under applied $J_{Pt} = 3.27 \times 10^{11}$ A m^{-2} ($J_{PtMn} = 8.17 \times 10^{10}$ A m^{-2}) for $\tau_P = 50$ μs, 1, 100 and 500 ms. (**b**) Experimental results of τ_P dependence of R_{Hall} for PtMn(10)/Ru structure for applied $J_{PtMn} = 2.62 \times 10^{11}$ A/m^2 with similar polarities of I_1 and I_2. Red and blue-rimmed circles correspond to applied I_1 and I_2, respectively. The polarities of $I_{1,2}$ are identical to that in Fig. 1.

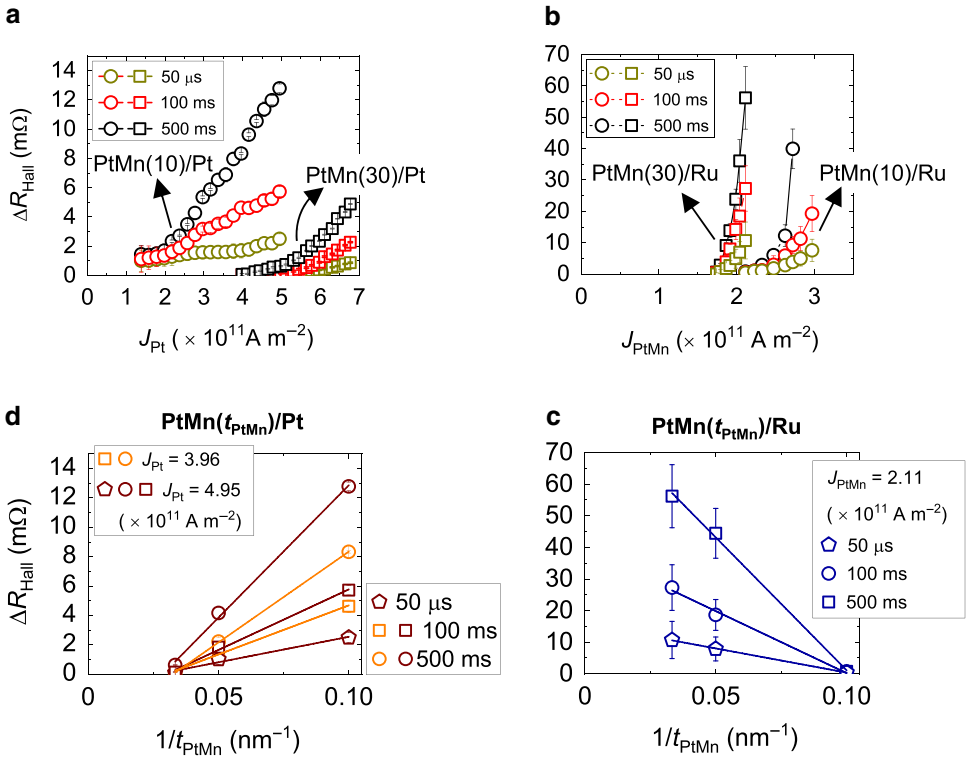

Fig. 3 AFM thickness dependence of current-induced switching in PtMn/Pt and PtMn/Ru structures. (**a**), (**b**) Dependence of the change in Hall resistance (ΔR_{Hall}) as a function of write current densities J_{Pt} and J_{PtMn} for PtMn(10 or 30)/Pt and PtMn(10 or 30)/Ru structures, respectively, for various pulse widths $\tau_P = 50$ μs, 100 ms and 500 ms. (**c**), (**d**) Inverse of AFM thickness (t_{PtMn}) dependence of ΔR_{Hall} for PtMn/Pt and PtMn/Ru, respectively. Solid lines in (**c**), (**d**) are guides to the eye.

To elucidate the effect of current, we then investigate τ_P dependence of switching in PtMn(t_{PtMn})/Pt and PtMn(t_{PtMn})/Ru structures. Figure 2a, b shows τ_P dependence of R_{Hall} for PtMn (10)/Pt and PtMn(10)/Ru for applied I_1 and I_2 along A(C)→ B (D). For both structures, application of I_1 and I_2 pulses changes R_{Hall}, consistent with an interpretation of current-induced switching or reorientation of the antiferromagnetic Néel vector. A decrease of τ_P from 500 to 1 ms results in a drastic reduction of the change in R_{Hall} while a further decrease to 50 μs results in a slight depreciation of R_{Hall}. The switching characteristics of PtMn (10)/Pt depend on current-polarity (see supplementary Fig. S4a, b) and distinctly differs from the sawtooth-like unipolar behavior in PtMn(10)/Ru (see Supplementary Fig. S5a). This sawtooth-like nature also persists for various τ_P and t_{PtMn} (see supplementary Fig. S5(b)–(d)), and closely resembles the switching characteristics observed in some previous works[40,41]. The present results suggest the existence of different driving forces, manifesting in distinct R_{Hall} characteristics of PtMn with/without the HM layer.

To capture the dynamics of current-induced switching, we summarize J_{Pt} or J_{PtMn} dependence of the change in Hall resistance (ΔR_{Hall}) for PtMn($10 \le t_{PtMn} \le 30$)/Pt and PtMn($10 \le t_{PtMn} \le 30$)/Ru (Fig. 3a, b, respectively). For both the structures, an increase of write current density (J_{Pt} or J_{PtMn}) or τ_P results in an increase of ΔR_{Hall}, irrespective of t_{PtMn}, indicating an increased degree of antiferromagnetic Néel vector manipulation in the presence of thermal effects (as shown later). However, closer inspection reveals further differences in ΔR_{Hall} versus J_{Pt} or J_{PtMn} between PtMn/Pt and PtMn/Ru structures, respectively. For PtMn/Pt structures, we find evidence of two distinct regimes of ΔR_{Hall} depending on the magnitude of J_{Pt}; low J_{Pt} regime ($J_{Pt} \le 2 \times 10^{11}$ and 5×10^{11} A m^{-2} for PtMn(10)/Pt and PtMn(30)/Pt, respectively) associated with minuscule changes in ΔR_{Hall} and a second regime evidencing larger changes of ΔR_{Hall}. For PtMn/Ru structures, unlike PtMn/Pt, we observe a sharp increase of ΔR_{Hall} confined within a small range of J_{PtMn}. A second difference arises in the t_{PtMn} dependence of threshold current between these two structures. The threshold current required for detectable switching of the antiferromagnetic Néel vector increases with increasing t_{PtMn} for PtMn/Pt structures, while showing the opposite trend for the PtMn/Ru alone. Furthermore, striking differences appear in the behavior of ΔR_{Hall} versus $1/t_{PtMn}$ for both structures for various applied write current densities and τ_P (Fig. 3c, d). An increase of t_{PtMn} for PtMn/Pt results in a decrease of ΔR_{Hall} whereas again showing an opposite behavior for PtMn/Ru. As discussed later, the former trend is expected from switching of the antiferromagnetic Néel vector by SOTs from the HM layer while the latter is likely from several origins, magnetic or non-magnetic. Nevertheless, our experimental results demonstrate the possibility of current-induced switching of antiferromagnetic PtMn with relatively low current densities of ~10^{11} A m^{-2} from dc to μs pulses, relevant for AFM-based future spintronic devices.

XMLD-PEEM imaging of current-induced switching in AFM/HM structures. To prove that the application of orthogonal write pulses indeed results in electrical switching characteristics of magnetic origin, we resort to XMLD-PEEM imaging of Pt/PtMn (10) structures. Separate electrical switching measurements confirm similar reversible current-induced switching behavior in these structures as well (see Supplementary Fig. S6). Domain imaging is carried out for both linear vertical (LV) and linear horizontal (LH) polarizations under the application of current, enabling the visualization of the magnetization configurations for high and low-resistive R_{Hall} states. Figure 4a–c shows the optical micrograph of the device structure along with the directions of

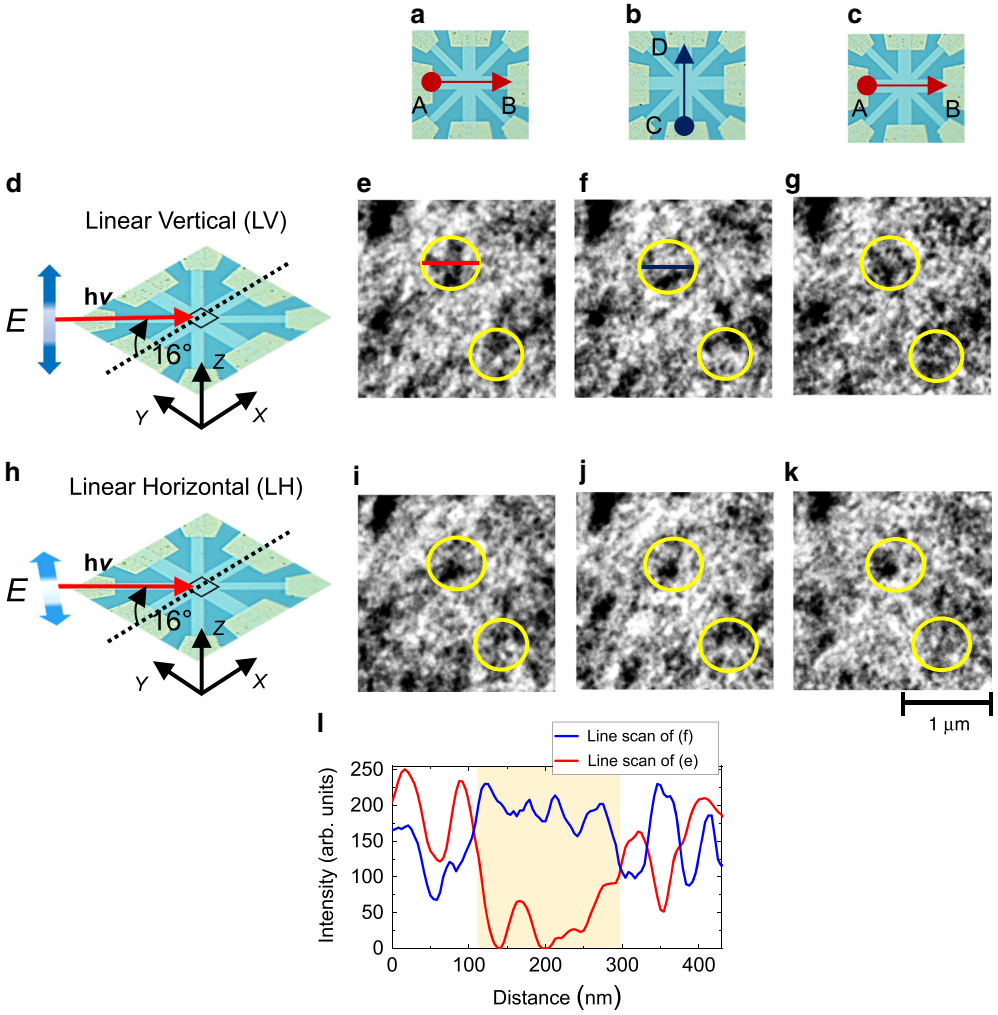

Fig. 4 XMLD-PEEM imaging of current-induced switching in Pt/PtMn(10) structures. (**a**)-(**c**) Schematic diagram of the sequence of applied write currents in Pt/PtMn(10). (**d**), (**h**) Schematic diagram of the measurement set-up for XMLD-PEEM imaging. X-rays are incident on the sample at an angle of 16° to the sample surface. Linear vertical (LV) and linear horizontal (LH) polarizations of the x-ray beam are indicated by thick blue arrows. The black square box of approximate size 2 μm × 2 μm at the center of the device denotes the position where the imaging was carried out. (**e**)-(**g**) LV polarization XMLD-PEEM images of Pt/PtMn(10) structure. The images were taken after injection of 20 pulses of 100 ms duration for $J_{Pt} = 5.93 \times 10^{11}$ A m^{-2} along A (B)→C(D). White and black areas in the figure indicate regions with opposite linear dichroism contrast for the LV polarization of the incident beam. Yellow circles highlight regions of the sample with prominent switching. (**i**)-(**k**) LH polarization XMLD-PEEM images at the same position as (**e**)-(**g**) after the application of current pulses. White and black areas in the figure indicate regions with opposite linear dichroism contrast for the LH polarization of the incident beam. Changes due to current pulsing are visible also in these images. (**l**) Line scan of pixel intensity (in arb. unit) vs distance for red and blue lines in panels (**e**) and (**f**), respectively. The switchable antiferromagnetic domain size under the action of the current is determined from the length of the yellow shaded region.

applied $I_{1,2}$ while Fig. 4d, h shows the schematic diagram of the measurement configuration. The linear polarization of the x-rays in the LH mode is in-plane, whereas that of the LV mode makes an angle of 16° with respect to the sample normal. Figure 4e–g, i–k shows the normalized XMLD images in LV and LH mode, respectively, after the injection of orthogonal write pulses of magnitude $J_{Pt} = 5.93 \times 10^{11}$ A m^{-2} and τ_P =100 ms. The XMLD asymmetry is obtained by subtracting images on and off the L_3 edge for each polarization (see Methods). Separate X-ray circular magnetic dichroism (XMCD) measurements at Mn L_3 edge on AFM/FM PtMn/[Co/Ni] multilayer structures do not reveal any discernable XMCD signals upon the application of current, ruling out any dominant contribution from disordered or uncompensated moments. Despite the possible presence of chemical and morphological contrast in both LV and LH configurations, which can be caused by variations in the stoichiometry and orientation of different crystal grains, we observe contrast reversal in several areas (black to white, and vice-versa) following current-induced switching. As seen in Fig. 4e–g, the application of orthogonal $I_{1,2}$ results in reversible changes, which we attribute to the reversal of the antiferromagnetic Néel vector. In addition, some areas do not show any contrast reversal either in LH or LV polarization, indicating non-switchable portions, as well. Precise identification of the dynamics of the antiferromagnetic Néel vector during electrical switching requires XMLD-PEEM imaging for various orientations of the sample with respect to the incident x-rays direction, which will be investigated in future. Figure 4l shows the line scans through the LV images in Fig. 4e, f. Discernible changes in antiferromagnetic Néel vector occur over a localized region with an upper limit of sizes in the range of hundreds of nm (shaded area in Fig. 4l), consistent with previous studies using different collinear antiferromagnetic structures[42,43]. We believe that the observed current-induced switching behavior is a universal feature and offers the possibility to utilize

polycrystalline metallic AFMs within the arena of antiferromagnetic spintronics.

Discussion

As presented above, we demonstrate current-induced 90° switching of the antiferromagnetic Néel vector in metallic AFM heterostructures. To understand the scenarios responsible for the observed switching behavior, we first address the issue of spin structure and magnetocrystalline anisotropy of PtMn. In bulk AFM crystals, PtMn has uniaxial anisotropy, which does not favor 90° switching. Our sputtered films, however, have a polycrystalline structure. Previous studies pointed out that significant magnetostriction coefficient[44] and the sensitivity of Mn-based AFMs to crystallinity and/or chemical composition[29,30,32,45] (e.g., effects of Mn substitution/doping and valence electron number) could induce an easy-plane magnetic anisotropy[46–48], resulting in multiple stable Néel vector orientations in the polycrystalline films. Note that our observation of a reversible XMLD contrast along LV and LH configurations (Fig. 4(e)–(k)) is also consistent with the above scenario, indicating the possibility of both out-of-plane and in-plane Néel vector components. Besides, to quantify the effect of interfacial chiral interactions[48,49] (e.g., Dzyaloshinskii-Moriya interaction (DMI)), we also estimate the DMI constant (D) (see supplementary Fig. S7). The estimated D is close to the threshold value[48] (see supplementary table T1) required for the generation of an inhomogeneous ground state with Néel-type domain wall (DW)[24,49–51], and/or other topological spins textures[52–54]. The DW width, estimated to be a few nm, is much smaller than the magnetic domain or crystallographic grain size (see Supplementary Fig. S8), indicating the feasibility of the above scenario. For a polycrystalline textured PtMn, these estimates intuitively imply the possible existence of an inhomogeneous multi-domain antiferromagnetic ground state configuration with a partial or dominant easy-plane magnetic anisotropy contribution, accounting for the observed 90° switching.

Next, we discuss the effect of possible interactions namely, the bulk or interfacial SOTs generated by spin-Hall effect in HM layer[22–24,26], Néel SOTs specific to the AFM[37–39], spin-transfer torque (STT) generated by spin-polarized conduction electrons in the AFM layer[55,56], and thermal activation of antiferromagnetic grains[20,41] due to the effect of Joule heating. Owing to the negligible current flow through the oxidized Ru capping layer, we do not consider its contribution for both PtMn/Pt and PtMn/Ru structures. The lack of structural inversion asymmetry in this collinear AFM is incompatible with the description of current-induced switching by staggered field-like Néel SOTs, originating from inverse spin galvanic effects, previously demonstrated in biaxial CuMnAs and Mn_2Au antiferromagnetic structures[7,8,18–21]. This rule out any presence of Néel SOTs, leading to the observed current-induced switching in both PtMn/Pt and PtMn/Ru structures. To understand the possible role of thermally-activated dynamics, we also quantify the temperature rise in PtMn/Pt and PtMn/Ru structures by using the device resistance as a thermometer probe (see supplementary Fig. S9a–d). The estimated rise in temperature of PtMn/Ru at maximum J is higher than 300 K (see supplementary Fig. S9b), whereas it reaches only ~100 K in PtMn/Pt (see supplementary Fig. S9d). This substantial increase of temperature in the PtMn/Ru structures is also accompanied by localized darkening/hot spots (see supplementary Fig. S10) and a non-negligible variation of ΔR_{Hall} from sample to sample. For PtMn/Ru, the current flowing through the AFM layer can also result in STTs acting on the multi-domain ground state. Theoretical calculations have shown that adiabatic and non-adiabatic components of STTs can lead to translational motion of AFM DWs[55,56], which could result in a magnetoresistive response owing to the finite magnetization in the DW region. For this scenario, the threshold current required to induce DW motion should remain unchanged with increasing t_{PtMn}, roughly consistent with our observed results (Fig. 3b). However, the non-saturating behavior of switching amplitude and its variation in successive cycles indicate intermingled contributions from other sources such as thermally activated reorientation of antiferromagnetic Néel vector[20,41] and/or non-magnetic contributions arising from electromigration[40]. Whereas our electrical measurements do not enable us to distinguish these factors, the present observations are likely related to a combination of thermally-activated reorientation of the antiferromagnetic Néel vector with possible contributions from STT and other non-magnetic effects. On the other hand, the opposite dependence of ΔR_{Hall} versus $1/t_{PtMn}$ for PtMn/Pt structures and a much smaller temperature rise suggest a different scenario. Owing to the significantly lower switching amplitude of PtMn/Ru as compared to PtMn/Pt at comparable J_{PtMn} (Fig.1g, i), we ignore any contributions from STTs, and only consider the effects of bulk or interfacial SOTs on the inhomogeneous multi-domain antiferromagnetic ground state for a qualitative understanding of the switching behavior. Note that the current-polarity dependent switching in our PtMn/Pt structures is significantly different from the unipolar characteristics in PtMn/Ru and to those previously observed in AFM-insulator NiO/HM structures[22–24,57], calling for additional factors leading to the observed results. As stated before, a combination of uniaxial and easy-plane anisotropies along with interfacial DMI can lead to the spontaneous multi-domain configuration comprising Néel DWs and/or topological spin textures[47,48,52–54] in PtMn/Pt structures. In fact, these predictions have been confirmed by recent experiments demonstrating imprinted antiferromagnetic vortex states on an adjacent ferromagnetic layer in AFM/FM[52,53] or exotic topological meron-antimeron pairs in AFM/HM structures[54]. The twisting of the antiferromagnetic Néel vector around these spin textures leads to non-zero Néel topological charge, endowing protected spin configurations with distinct magnetic polarities and chiralities (sizes ~ hundreds of nm) and robust thermal stability. Besides, numerical simulations also suggest efficient nucleation and motion of these antiferromagnetic spin textures under the action of SOTs in AFM/HM[58]. Thus, a possible scenario concerning the polarity dependent current-induced switching characteristics is attributed to the action of SOTs on the inhomogeneous multi-domain configuration. Irrespective of the initial multi-domain configuration, the switching dynamics is expected to proceed via a 90° rotation of the in-plane projection of Néel vector towards the spin-polarization direction[48] by rearrangement or motion of DWs, and/or current-induced nucleation and motion of vortex-antivortex pairs, skyrmions, or bimerons[54,58]. An increase of the switching amplitude (ΔR_{Hall}) versus J_{Pt} is attributed to enhanced current-induced nucleation or rearrangement of these spin textures, whereas the partial switching might be due to pinning effects. In principle, the threshold-like behavior observed in ΔR_{Hall} versus J_{Pt}, can be attributed to the cross-over between various regimes of spin texture dynamics characterized by different pinning strengths. Furthermore, an increase of t_{PtMn} above the spin-diffusion length results in decreased efficiencies of SOTs and lower probability of switching, similar to the ferromagnetic case. Contrary to the common understanding that biaxial AFMs are required for electrical switching, our results demonstrate the potential of polycrystalline antiferromagnetic metals compatible with existing complementary metal-oxide semiconductor (CMOS) technology for low current operation and high thermal stability antiferromagnetic spintronics. We also believe that the present results indicate an intricate role played by topological

spin textures for current-induced switching and points towards an unexplored pathway for their utilization in future antiferromagnetic spintronic devices.

In summary, we demonstrate SOT-induced switching of the Néel vector in a Mn-based metallic AFM/HM heterostructure at low current densities of $\approx 10^{11}$ A m^{-2} from dc to μs regime. The comparison of the electrical measurements in AFM structures with and without the HM layer allows us to distinguish different current-induced effects in AFMs. The combination of electrical measurements with x-ray imaging clearly shows reversible switching characteristics of the antiferromagnetic Néel vector within localized regions of sizes of hundreds of nm. The large Δ for the antiferromagnetic PtMn ensures a stable Néel vector orientation, implying robust data retention capabilities of this material system. The present study shows that polycrystalline metallic AFM/HM structures are promising candidates for antiferromagnetic spintronics.

Method

Film preparation. The films were deposited at room temperature onto 3-inch high-resistive Si wafers with a natural oxidation layer. RF magnetron sputtering was used to deposit the MgO layer, and DC magnetron sputtering was used to deposit the other layers. Base pressure of the chamber was less than 1×10^{-6} Pa, and Ar gas was used for sputtering. No magnetic field was applied during the sputtering. The composition of PtMn sputtering target is $Pt_{38}Mn_{62}$ (in atomic %).

Device fabrication. The deposited films of Ta(3)/Pt(3)/ MgO(2)/PtMn(t_{PtMn})/Pt (5)/Ru(1) and Ta(3)/Pt(3)/ MgO(2)/PtMn(t_{PtMn})/Ru(1) were processed into star-shaped devices by photolithography and Ar ion milling. Electrodes and contact pads made of Cr (5 nm)/Au (100 nm) were formed by photolithography and lift-off. Width and length of the write channel of the star-shaped devices were 10 and 60 μm, respectively, and those of the read channel were 5 and 60 μm, respectively. After the fabrication, the samples were annealed at 300 °C for two hours under an in-plane magnetic field of 1.2 T directed parallel to the write channel. Resistivities of Ta, Pt, and $Pt_{0.38}Mn_{0.62}$ layers were determined from separate measurements of sheet resistance on annealed blanket films and is reported elsewhere[17].

XMLD-PEEM measurements. X-ray absorption spectroscopy and XMLD-PEEM experiments, with 10 μm field of view, were performed at the I06 beamline at the Diamond Light Source, UK. PEEM images were acquired with x-ray energies at $E_1 = 638.15$ eV and $E_2 = 638.95$ eV, incident at an angle of 16° on the sample surface (schematic of the measurement is shown in Fig. 4). E_2 and E_1 correspond to the energies closer to the Mn L_3 edge at which the maximum XMLD contrast is obtained, resulting in a difference in absorption between regions with spin-axis collinear or perpendicular to the incident x-ray polarization[59]. XMLD images were obtained by calculating the normalized difference of consecutive images measured at $E_{1,2}$, that is, by calculating the intensity of each pixel as $[i(E_1) - i(E_2)]/[i(E_1) + i(E_2)]$. The images were acquired for both linear vertical (LV) and linear horizontal (LH) polarization of the incident x-rays, before and after the application of current pulses. Note that, in addition to the XMLD effect, the intensity asymmetry calculated by subtracting images on and off the L_3 edge also depends on local variations of the x-ray absorption intensity due to the different stoichiometry and orientation of the PtMn crystal grains. Contrast changes following the application of current pulses, however, are purely of magnetic origin.

Data availability

The data which support the findings of this work are available from the corresponding author upon reasonable request.

Received: 16 March 2020; Accepted: 14 October 2020;
Published online: 11 November 2020

References

1. MacDonald, A. H. & Tsoi, M. Antiferromagnetic metal spintronics. *Philos. Trans. R. Soc. A* **369**, 3098–3114 (2011).
2. Jungwirth, T., Marti, X., Wadley, P. & Wunderlich, J. Antiferromagnetic spintronics. *Nat. Nanotech.* **11**, 231–241 (2016).
3. Fukami, S., Zhang, C., DuttaGupta, S., Kurenkov, A. & Ohno, H. Magnetization switching by spin-orbit torque in an antiferromagnet-ferromagnet bilayer system. *Nat. Mater.* **15**, 535–541 (2016).
4. Oh, Y. W. et al. Field-free switching of perpendicular magnetization through spin-orbit torque in antiferromagnet/ferromagnet/oxide structures. *Nat. Nanotech.* **11**, 878–884 (2016).
5. Baltz, V. et al. Antiferromagnetic spintronics. *Rev. Mod. Phys.* **90**, 015005 (2018).
6. Železný, J., Wadley, P., Olejník, K., Hoffmann, A. & Ohno, H. Spin transport and spin torque in antiferromagnetic devices. *Nat. Phys.* **14**, 220–228 (2018).
7. Wadley, P. et al. Electrical switching of an antiferromagnet. *Science* **351**, 587–590 (2016).
8. Olejník, K. et al. Antiferromagnetic CuMnAs multi-level memory cell with microelectronic capability. *Nat. Commun.* **8**, 15434 (2017).
9. Borders, W. A. et al. Analogue spin-orbit torque device for artificial-neural-network-based associative memory operation. *Appl. Phys. Express* **10**, 013007 (2017).
10. Kurenkov, A. et al. Artificial neuron and synapse realized in an antiferromagnet/ferromagnet heterostructure using dynamics of spin-orbit torque switching. *Adv. Mater.* **31**, 1900636 (2019).
11. Barker, J. & Tretiakov, O. A. Static and dynamical properties of antiferromagnetic skyrmions in the presence of applied current and temperature. *Phys. Rev. Lett.* **116**, 147203 (2016).
12. Manchon, A. et al. Current-induced spin-orbit torques in ferromagnetic and antiferromagnetic systems. *Rev. Mod. Phys.* **91**, 035004 (2019).
13. Kurenkov, A., Fukami, S. & Ohno, H. Neuromorphic computing with antiferromagnetic spintronics. *J. Appl. Phys.* **128**, 010902 (2020).
14. Hoogeboom, G. R., Aqeel, A., Kuschel, T., Palstra, T. T. M. & van Wees, B. J. Negative spin Hall magnetoresistance of Pt on the bulk easy-plane antiferromagnet NiO. *Appl. Phys. Lett.* **111**, 052409 (2017).
15. Fischer, J. et al. Spin Hall magnetoresistance in antiferromagnet/heavy-metal heterostructures. *Phys. Rev. B.* **97**, 014417 (2018).
16. Baldarati, L. et al. Full angular dependence of spin Hall and ordinary magnetoresistance in epitaxial antiferromagnetic NiO (001)/Pt thin films. *Phys. Rev. B.* **98**, 024422 (2018).
17. DuttaGupta, S., Itoh, R., Fukami, S. & Ohno, H. Angle dependent magnetoresistance in heterostructures with antiferromagnetic and non-magnetic metals. *Appl. Phys. Lett.* **113**, 202404 (2018).
18. Bodnar, S. Y. et al. Writing and reading of antiferromagnetic Mn_2Au by Néel spin-orbit torques and large anisotropic magnetoresistance. *Nat. Commun.* **9**, 348 (2018).
19. Wadley, P. et al. Current-polarity-dependent manipulation of antiferromagnetic domains. Nature. *Nat. Nanotechnol.* **13**, 362 (2018).
20. Meinert, M., Graulich, D. & Mallata-Wagner, T. Electrical switching of antiferromagnetic Mn_2Au and the role of thermal activation. *Phys. Rev. Appl.* **9**, 064040 (2018).
21. Zhou, X. F. et al. Strong orientation-dependent spin-orbit torque in thin films of the antiferromagnet Mn_2Au. *Phys. Rev. Appl.* **9**, 054208 (2018).
22. Chen, X. Z. et al. Antidamping-torque-induced switching in biaxial antiferromagnetic insulators. *Phys. Rev. Lett.* **120**, 207204 (2018).
23. Moriyama, T., Oda, K., Ohkochi, T., Kimata, M. & Ono, T. Spin torque control of antiferromagnetic moments in NiO. *Sci. Rep.* **8**, 14167 (2018).
24. Baldrati, L. et al. Mechanism of Néel order switching in antiferromagnetic thin films revealed by magnetotransport and imaging techniques. *Phys. Rev. Lett.* **123**, 177201 (2019).
25. Chen, X. et al. Electric field control of Néel spin-orbit torque in an antiferromagnet. *Nat. Mater.* **18**, 931 (2019).
26. Zhou, X. F. et al. From fieldlike torque to antidamping torque in antiferromagnetic Mn_2Au. *Phys. Rev. Appl.* **11**, 054030 (2019).
27. Kašpar, Z. et al. High resistive unipolar-electrical and fs-optical switching in a single layer antiferromagnetic memory, arXiv:1909.09071 (2019).
28. Wörnle, M. S. et al. Current-induced fragmentation of antiferromagnetic domains, arXiv:1912.05287v1 (2019).
29. Krén, E. et al. Magnetic structures and exchange interactions in the Mn-Pt system. *Phys. Rev.* **171**, 574 (1968).
30. Sakuma, A. First-principles study on the non-collinear magnetic structures of disordered alloys. *J. Phys. Soc. Jpn.* **69**, 3072 (2000).
31. Nozières, J. P. Blocking temperature distribution and long-term stability of spin-valve structures with Mn-based antiferromagnets. *J. Appl. Phys.* **87**, 3920 (2000).
32. Umetsu, R. Y., Sakuma, A. & Fukamichi, K. Magnetic anisotropy energy of antiferromagnetic L10-type equiatomic Mn alloys. *Appl. Phys. Lett.* **89**, 052504 (2006).
33. Ladwig, F. P., Chang & Austin, Y. Paramagnetic to antiferromagnetic phase transformation in sputter deposited Pt-Mn thin films. *J. Appl. Phys.* **94**, 979 (2003).
34. Kurenkov, A., Zhang, C., DuttaGupta, S., Fukami, S. & Ohno, H. Device-size dependence of field-free spin-orbit torque induced magnetization switching in antiferromagnet/ferromagnet structures. *Appl. Phys. Lett.* **110**, 092410 (2017).
35. Miron, I. M. et al. Perpendicular switching of a single ferromagnetic layer induced by in-plane current injection. *Nature* **476**, 189–193 (2011).

36. Liu, L., Lee, O. J., Gudmundsen, T. J., Ralph, D. C. & Buhrman, R. Current-induced switching of perpendicularly magnetized magnetic layers using spin torque from the spin hall effect. *Phys. Rev. Lett.* **109**, 096602 (2012).
37. Železný, J. et al. Relativistic Néel-order fields induced by electrical current in antiferromagnets. *Phys. Rev. Lett.* **113**, 157201 (2014).
38. Roy, P. E., Otxoa, R. M. & Wunderlich, J. Robust picosecond writing of a layered antiferromagnet by staggered pin-orbit fields. *Phys. Rev. B.* **94**, 014439 (2016).
39. Šmejkal, L., Železný, J., Sinova, J. & Jungwirth, T. Electric control of dirac quasiparticles by spin-orbit torque in an antiferromagnet. *Phys. Rev. Lett.* **118**, 106402 (2018).
40. Chiang, C. C., Huang, S. Y., Qu, D., Wu, P. H. & Chien, C. L. Absence of evidence of electrical switching of the antiferromagnetic Néel vector. *Phys. Rev. Lett.* **123**, 227203 (2019).
41. Cheng, Y., Yu, S., Hwang, J. & Yang, F. Electrical switching of tristate antiferromagnetic Néel order in α-Fe_2O_3 epitaxial films. *Phys. Rev. Lett.* **124**, 027202 (2020).
42. Grzybowski, M. J. et al. Imaging current-induced switching of antiferromagnetic domains in CuMnAs. *Phys. Rev. Lett.* **118**, 057701 (2017).
43. Bodnar, S. Y. et al. Imaging of current induced Néel vector switching in antiferromagnetic Mn_2Au. *Phys. Rev. B.* **99**, 140409(R) (2019).
44. Park, I. J. et al. Strain control of the Néel vector in Mn-based antiferromagnets. *Appl. Phys. Lett.* **115**, 142403 (2019).
45. Andresen, A., Kjekshus, A., Møllerud, R. & Pearson, W. B. Equiatomic transition metal alloys of manganese IV. A neutron diffraction study of magnetic ordering in the PtMn phase. *Philos. Mag.: A J. Theor. Exp. Appl. Phys.* **11**, 1245 (1965).
46. Solina, D. et al. The magnetic structure of L10 ordered MnPt at room temperature determined using polarized neutron diffraction. *Mater. Res. Express* **6**, 076105 (2019).
47. Shi, J. et al. Electrical manipulation of the magnetic order in antiferromagnetic PtMn pillars. *Nat. Elec.* **3**, 92 (2020).
48. Tomasello, R. et al. Domain periodicity in an easy-plane antiferromagnet with Dzyaloshinskii-Moriya interaction. arXiv:2004.01944 (2020).
49. Sanchez-Tejerina, L., Puliafito, V., Amiri, P. K., Carpentieri, M. & Finocchio, G. Dynamics of domain-wall motion driven by spin-orbit torques in antiferromagnets. *Phys. Rev. B.* **101**, 014433 (2020).
50. Gomonay, O., Jungwirth, T. & Sinova, J. High antiferromagnetic domain wall velocity induced by Néel spin-orbit torques. *Phys. Rev. Lett.* **117**, 017202 (2016).
51. Shiino, T. et al. Antiferromagnetic domain wall motion driven by spin-orbit torques. *Phys. Rev. Lett.* **117**, 087203 (2016).
52. Wu, J. et al. Direct observation of imprinted antiferromagnetic vortex states in CoO/Fe/Ag(001) discs. *Nat. Phys.* **7**, 303 (2011).
53. Chmiel, F. P. et al. Observation of magnetic vortex pairs at room temperature in a planar α-Fe_2O_3/Co heterostructure. *Nat. Mater.* **17**, 581 (2018).
54. Jani, H. et al. Half-skyrmions and Bimerons in an antiferromagnetic insulator at room temperature. arXiv:2006.12699v (2020).
55. Xu, Y., Wang, S. & Xia, K. Spin-transfer torques in antiferromagnetic metals from first principles. *Phys. Rev. Lett.* **100**, 226602 (2008).
56. Tveten, E. G., Qaiumzadeh, A., Tretiakov, O. A. & Brataas, A. Staggered dynamics in antiferromagnets by collective coordinates. *Phys. Rev. Lett.* **110**, 127208 (2013).
57. Gray, I. et al. Spin seeback imaging of spin-torque switching in antiferromagnet Pt/NiO heterostructures. *Phys. Rev. X* **9**, 041016 (2019).
58. Shen, L. et al. Current- induced dynamics and chaos of antiferromagnetic bimerons. *Phys. Rev. Lett.* **124**, 037202 (2020).
59. Fujii, J. et al. Evidence for in-plane spin-flop orientation at the MnPt/Fe (100) interface revealed by x-ray magnetic linear dichroism. *Phys. Rev. B.* **73**, 214444 (2006).

Acknowledgments

We thank C. Igarashi, T. Hirata, H. Iwanuma, and K. Goto for their technical support and Dr. J. Llandro for discussions. A portion of this work was supported by the JSPS KAKENHI 17H06511, 18KK0143, 19H05622, and Cooperative Research Projects of RIEC. O.A.T. acknowledges support by the Australian Research Council (Grant No. DP200101027), the Cooperative Research Project Program at the Research Institute of Electrical Communication, Tohoku University, and by the NCMAS 2020 grant. G.K., G.S., and P.G. acknowledge funding from the Swiss National Science Foundation (Grant No. 200020-172775). V.K. was supported by a Swiss Government Excellence Scholarship.

Author contributions

S.D. and S.F. planned the study. S.D. deposited the films and fabricated the samples. S.D. performed the electrical measurements and analyzed the data with inputs from A.K. and O.A.T. A.K., G.K., G.S., V.K., and F.M. measured and analyzed the XMLD data with input from P.G. S.D. wrote the manuscript with input from all the authors. All authors discussed the results.

Competing interests

The authors declare no competing interests.

Additional information

Supplementary information is available for this paper at https://doi.org/10.1038/s41467-020-19511-4.

Correspondence and requests for materials should be addressed to S.D.

Peer review information *Nature Communications* thanks Olena Gomonay and the other, anonymous, reviewer(s) for their contribution to the peer review of this work. Peer reviewer reports are available.

Reprints and permission information is available at http://www.nature.com/reprints

Publisher's note Springer Nature remains neutral with regard to jurisdictional claims in published maps and institutional affiliations.

Spin-orbit torque switching of an antiferromagnetic metallic heterostructure

Samik DuttaGupta[1-3]*, A. Kurenkov[1-3], Oleg A. Tretiakov[4], G. Krishnaswamy[5], G. Sala[5], V. Krizakova[5], F. Maccherozzi[6], S. S. Dhesi[6], P. Gambardella[5], H. Ohno[1-3,7,8] and S. Fukami[1-3,7,8]

[1]Center for Science and Innovation in Spintronics, Tohoku University, 2-1-1 Katahira, Aoba-ku, Sendai 980-8577, Japan
[2]Center for Spintronics Research Network, Tohoku University, 2-1-1 Katahira, Aoba-ku, Sendai 980-8577, Japan
[3]Laboratory for Nanoelectronics and Spintronics, Research Institute of Electrical Communication, Tohoku University, 2-1-1 Katahira, Aoba-ku, Sendai 980-8577, Japan
[4] School of Physics, The University of New South Wales, Sydney 2052, Australia
[5]Laboratory for Magnetism and Interface Physics, Department of Materials, ETH Zurich, 8093 Zurich, Switzerland
[6]Diamond Light Source, Chilton, Didcot, Oxfordshire, OX11 0DE, United Kingdom
[7]Center for Innovative Integrated Electronic Systems, Tohoku University, 468-1 Aramaki Aza Aoba, Aoba-ku, Sendai 980-0845 Japan
[8]WPI Advanced Institute for Materials Research, Tohoku University, 2-1-1 Katahira, Aoba-ku, Sendai 980-8577, Japan
**Corresponding author:* sdg@riec.tohoku.ac.jp

SUPPLEMENTARY INFORMATION

S1. X-ray diffraction (XRD) of PtMn thin films

The phase diagram for bulk PtMn around Mn-composition 40-65% shows three possible, stable crystallographic phases: a high-temperature liquid phase, chemically ordered B2 phase within the temperature range 1100-1700 K, and a chemically ordered antiferromagnetic $L1_0$ phase below 1100 K [S1]. In thin film form, it is widely known that sputter-grown as-deposited PtMn is paramagnetic with a disordered, face-centered-cubic (fcc) structure [S2, S3]. A post deposition annealing is required to transform it to antiferromagnetic $L1_0$-ordered phase with a face-centered-tetragonal (fct) structure, manifested as a gradual shift the XRD peaks associated with a change in lattice spacings [S2]. Note that the effect of post-deposition annealing is only to provide the necessary activation energy required for atomic rearrangement. To clarify the crystalline orientation of the antiferromagnet (AFM) PtMn, we carry out out-of-plane (θ - 2θ) XRD measurements using Ta(3)/Pt(3)/MgO(2)/PtMn(10)/Ru(2) structures for both as-deposited and annealed states. Figure 1 shows the XRD scans for as-deposited films and films annealed at 300 °C for 2 hr in the presence of an in-plane magnetic field. Only reflections from fcc or fct-PtMn(111) and fcc-Pt(111) are observed, indicating that PtMn and Pt layers have (111) orientation of fcc (or $L1_0$-ordered fct for PtMn) phase. Clearly, the (111) planar spacings changes from 2θ= 39.80° ± 0.02° for the as-deposited to 2θ= 40.20° ± 0.02° for the annealed thin films. This shift of the (111) peak position is expected to originate from the phase transformation from disordered fcc to $L1_0$-ordered tetragonal structures. While we cannot exactly quantify the degree of phase transformation in our thin films, we would like to point out that the observed 2θ value of 40.20° ± 0.02° matches with the one expected after completion of volume phase transformation [S2].

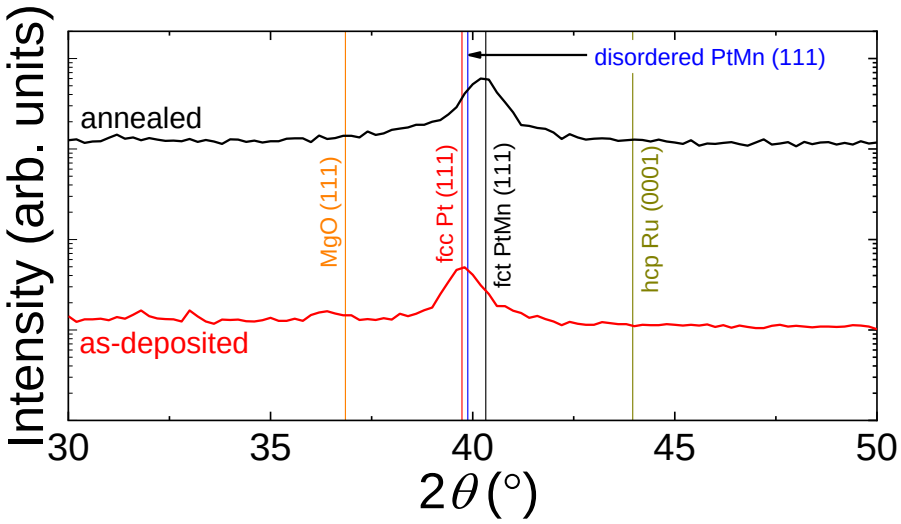

Figure S1: Out-of-plane X-ray diffraction (XRD) patterns for Ta(3)/Pt(3)/MgO(2)/PtMn(10)/Ru(2) heterostructures in as-deposited and annealed state, respectively. Annealing conditions are the same as mentioned in the main text. Vertical lines in the figure denotes the expected peak positions for (from left) MgO (111), fcc-Pt (111), disordered fcc-PtMn (111), fct-PtMn (111) and hcp-Ru (0001).

S2. Current-induced switching of PtMn(30)/Pt structures

In the main manuscript, we have demonstrated current-induced switching of antiferromagnetic Néel vector by spin-orbit torques (SOT) in PtMn(10)/Pt structures. To clarify the role of AFM in the current-induced switching of AFM/heavy-metal (HM) heterostructures, we have carried out electrical measurements on PtMn(t_{PtMn})/Pt structures for various PtMn thicknesses (t_{PtMn}). Figures S2 (a) and (b) show the experimental results of applied current-density and pulse width (τ_P) dependence of switching with an increase of t_{PtMn} up to ~ 30 nm in PtMn(30)/Pt structures of identical device dimensions as mentioned in the main text. Distinct reversible resistive modulation of the Hall resistance (R_{Hall}) under the application of orthogonal current pulse injection persists with an increase of t_{PtMn}. Similar to PtMn(10)/Pt, the degree of current-induced switching (ΔR_{Hall}) of the AFM increases with the increase of applied write current density in the Pt layer (J_{Pt}) and τ_P. The independence of the observed results with a variation of t_{PtMn} indicates the intrinsic nature of the observed behavior for PtMn(t_{PtMn})/Pt structures.

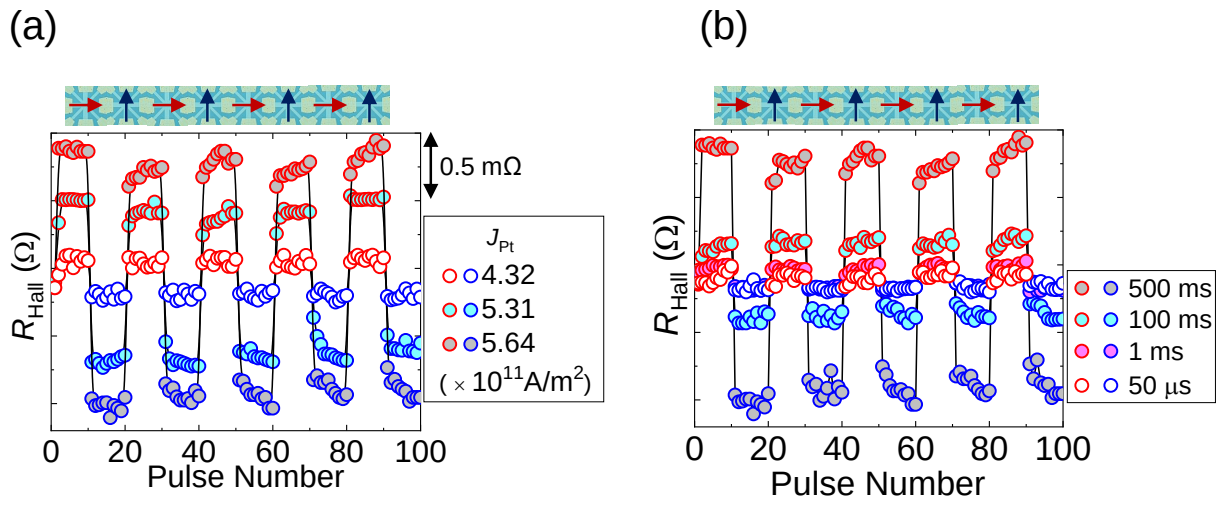

Figure S2: (a) Experimental results of current-induced switching of PtMn(30)/Pt structures under applied write current densities (J_{Pt}) = 4.32 ×10^{11} A/m^2 (J_{PtMn} = 4.96 × 10^{10} A/m^2), 5.31 × 10^{11} A/m^2 (J_{PtMn} = 5.95 × 10^{10} A/m^2) and 5.64 ×10^{11} A/m^2 (J_{PtMn} = 8.17 × 10^{10} A/m^2). (b) Pulse width dependence of Hall resistance (R_{Hall}) of the same structure under applied J_{Pt} = 5.64 ×10^{11} A/m^2. Schematic diagrams above fig. (b) indicate the direction of the applied write current pulses. Scale bar for the vertical axis is the same for both (a) and (b).

S3. Comparison of electrical switching characteristics between PtMn(10)/Pt and Pt(5) structures

Our experimental results on PtMn(10)/Pt and PtMn(10) structures demonstrate electrical writing of information in the metallic AFM by spin-orbit torques (SOTs). However, recent experimental results in AFM/HM structures have pointed towards thermoelectric origins of the observed voltage/resistance changes, not related to any changes of the antiferromagnetic Néel vector [S4]. To clarify the origin of the observed changes in Hall resistance (R_{Hall}), we compare our experimental results in sub./Ta(3)/Pt(2)/MgO(2)/PtMn(10)/Pt(5)/Ru(1) (PtMn(10)/Pt, hereafter) with similar experiments in sub./Ta(3)/Pt(5)/Ru(1) (Pt(5)/Ru, hereafter) structures. The deposited Pt(5)/Ru films were patterned into similar 8-terminal device structures (as in the main text). Five current pulses are sourced along the horizontal arm (A → B), followed by five pulses in the transverse direction (C → D). The polarities of $I_{1,2}$ are the same as the experimental configuration in the main text. Figures S3(a) and (b) shows the experimental results of current-induced switching in PtMn(10)/Pt and Pt(5)/Ru, respectively. Miniscule changes in R_{Hall} are observed for Pt(5)/Ru structure as compared to PtMn(10)/Pt for comparable magnitudes of applied write current densities in the Pt layer. This excludes the possibility of a dominant contribution of thermoelectric voltages to the observed R_{Hall} in PtMn/Pt structures.

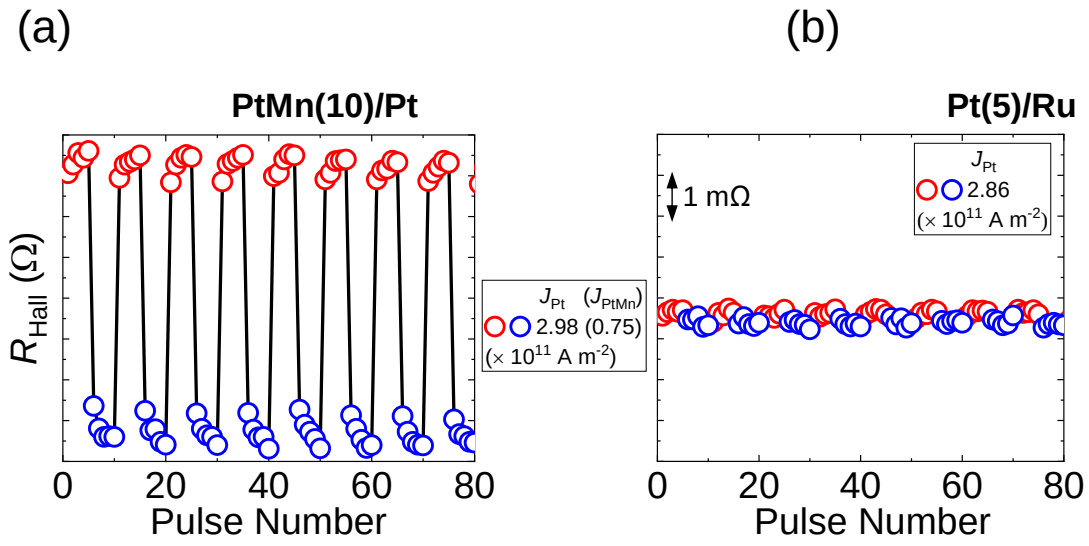

Figure S3: (a) Experimental results of current-induced switching of PtMn(10)/Pt structures under applied write current densities (J_{Pt}) = 2.98 ×10^{11} A/m^2 (J_{PtMn} = 7.51 × 10^{10} A/m^2). (b) Experimental results of similar measurements in Pt(5)/Ru structures under applied current densities (J_{Pt}) = 2.86 ×10^{11} A/m^2. Scale bar for the vertical axis is the same for both (a) and (b).

S4. Current-polarity dependence of switching in PtMn(t_{PtMn})/Pt structures

Our experimental results on PtMn/Pt and PtMn/Ru structures indicate a different origin of the current-induced switching characteristics, highlighting the different effects of the current between these structures. Here, we show a second distinct feature of the current-induced switching behavior in PtMn/Pt structures. Figure S4 (a) and (b) show the experimental results of current-induced switching experiments for various τ_P in PtMn(10)/Pt and PtMn(30)/Pt structures, respectively. The polarities of I_1 and I_2 are along D(B)→ C(A), as opposed to A(C)→ B(D) in the main text and supplementary section S1. A reversal of $I_{1,2}$ polarities results in a reversal of R_{Hall} for the PtMn/Pt structure. Interestingly, this bi-polar nature of current-induced switching is completely absent in PtMn structures without the HM layer (as will be shown in supplementary S5). While the origin of this behavior is still not well understood at present, we note that current-polarity dependent switching has been previously observed in CuMnAs, which was attributed to the current-induced motion of the antiferromagnetic domain walls (DWs) [S5]. A second possible origin for the observed behavior relates to the complicated roles played by uncompensated surface moments or possible non-collinear spin structures [S6, S7].

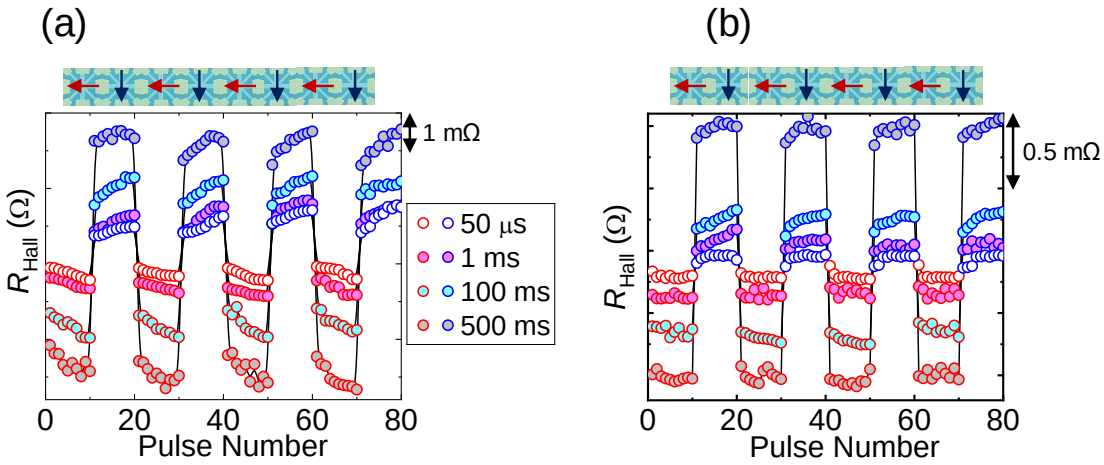

Figure S4: (a) Experimental results of current-induced manipulation of PtMn(10)/Pt structures under applied write current densities J_{Pt} = 3.27 ×10^{11} A/m^2 (J_{PtMn} = 8.17 × 10^{10} A/m^2) for pulse widths (τ_P) = 50 µs, 1 ms, 100 and 500 ms. Write current polarities are indicated in the schematics above the figures and opposite to that shown in the main text. (b) Pulse width dependence of current-induced switching of PtMn(30)/Pt structure under applied J_{Pt} = 5.64 ×10^{11} A/m^2 (J_{PtMn} = 8.17 × 10^{10} A/m^2). Schematic diagrams above fig. (b) indicate the direction of the applied write current pulses. Reversal of Hall resistance (R_{Hall}) is observed with the reversal of write current polarities irrespective of the thickness of the antiferromagnetic layer.

S5. Current-induced manipulation of PtMn(10 and 30)/Ru structures

The injection of current through the metallic AFM/HM heterostructure results in a finite current flow through both the AFM and NM layers. Different dynamics of magnetization can be induced owing to the current flow through the HM and the AFM layer [S8- S13]. Thus, understanding the current-induced manipulation results for AFM/HM structures also requires the quantification of current-induced effects on the AFM itself. Here, we experimentally evaluate the impact of current in sub./Ta(3)/Pt(2)/MgO(2)/PtMn(t_{PtMn})/Ru(1) (PtMn(t_{PtMn})/Ru, hereafter) structures. The device structure and the experimental configuration are identical to the one as mentioned in the main text. Write pulses ($I_{1,2}$) are injected along two orthogonal directions, and the transverse Hall resistance (R_{Hall}) is measured. Figure S5(a) and (b) show the experimental results of current-induced manipulation of PtMn(10)/Ru and PtMn(30)/Ru structures while S5(c) and (d) show the pulse width dependence of switching for these structures respectively. In contrast to the experimental results on AFM/HM structures, R_{Hall} shows a linear non-saturating increase (decrease) with the application of successive current pulses along I_1 (I_2). A change in write pulse amplitude results in an increase of R_{Hall} for both the structures, indicative of current-induced effects of the AFM. The different dynamics of the antiferromagnetic heterostructure under the application of current is indicative of different underlying dynamics of the antiferromagnetic Néel vector for AFM/HM and AFM heterostructures. Figure S5(c) and (d) show the τ_P dependence of R_{Hall} for PtMn(30)/Ru heterostructure under applied current density $J_{PtMn} = 2.11 \times 10^{11}$ A/m^2 with a change in the direction of the write pulses (→↑ and ←↓) as mentioned in the insets. As opposed to the experimental results on AFM/HM structures, the nature of R_{Hall} is insensitive to the direction of current in PtMn/Ru heterostructures. The present results highlight different underlying factors for antiferromagnetic Néel vector manipulation between PtMn/Pt and PtMn/Ru heterostructures. The underlying differences in the current-induced manipulation of these structures are discussed in the main text.

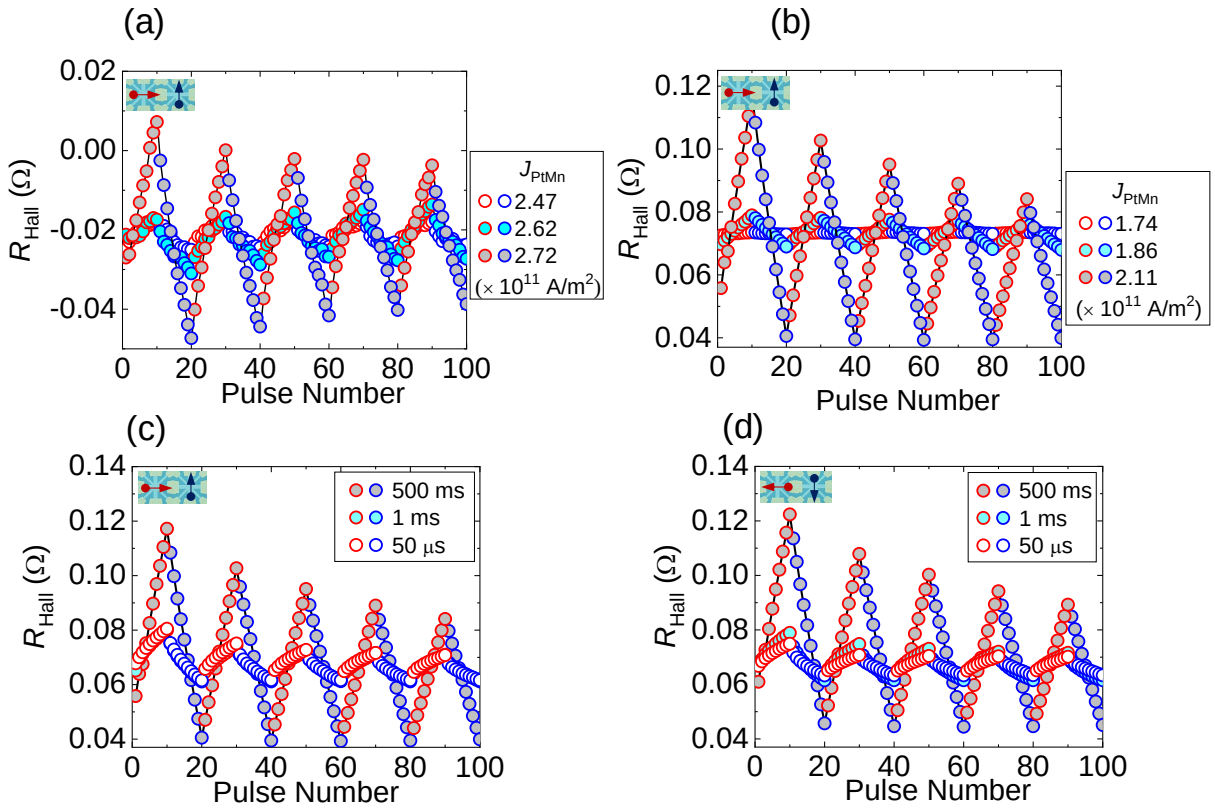

Figure S5: (a), (b) Experimental results of current-induced manipulation of PtMn(10)/Ru and PtMn(30)/Ru structures under applied write current pulses J_{PtMn} of 500 ms duration. Schematic micrographs above the figures indicate the direction of applied current pulses. A gradual triangular variation of the Hall resistance (R_{Hall}) is observed as opposed to the step-like behavior for PtMn/Pt structures. (c),(d) Pulse width dependence of Hall resistance (R_{Hall}) for PtMn(30)/Ru structure under applied write current J_{PtMn} = 2.11 $\times 10^{11}$ A/m^2 for opposite directions of the write current pulses. The schematic micrographs in the figure indicate the direction of the applied write current pulse.

S6. Current-induced switching of PtMn(10)/Pt structure utilized for X-Ray Magnetic Linear Dichroism (XMLD) measurements

Electrical measurements of current-induced switching were also carried out in the AFM/HM samples utilized for XMLD investigations. The device size and experimental configuration are identical to the one, as mentioned in the main text. Separate devices fabricated from the same wafer were utilized for XMLD measurements indicated in the main text. Figure S6 shows the experimental results of Hall resistance (R_{Hall}) under orthogonal current pulse injection at writing current densities of $J_{Pt} = 5.93 \times 10^{11}$ A/m^2 for applied pulse widths of 100 and 500 ms respectively. Similar bi-stable resistive states are obtained under the injection of current pulses, as shown in the main text. The present results confirm the reproducibility of the electrical measurements and enable a visualization of the antiferromagnetic dynamics under current-pulse injection.

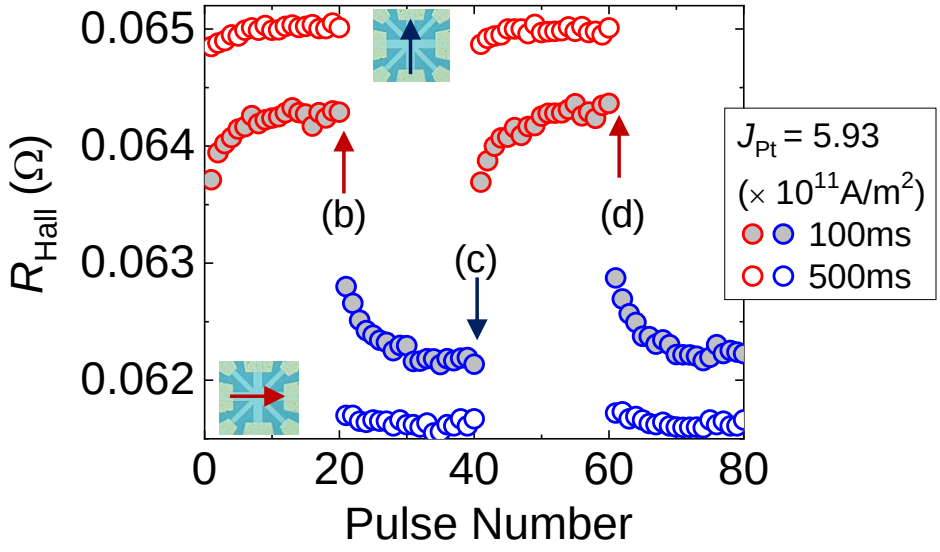

Figure S6: Experimental results of current-induced switching of Pt/PtMn(10) structures under orthogonal write pulse injection at current densities of J_{Pt} = 2.11 ×10^{11} A/m^2 for 100 and 500 ms pulse durations. Schematic micrographs shown inside the figure indicate the direction of the applied write pulse in a four-terminal geometry. Arrows in the figure indicate the position on the curve where the XMLD data is acquired and shown the main text (Fig.4 of the main text).

S7. Estimation of Dzyaloshinskii-Moriya constant (*D*) for PtMn/Pt structures

The clarification of Dzyaloshinskii-Moriya interaction (DMI) at AFM/HM interfaces and estimation of DMI constant (*D*) is expected to provide crucial insights concerning current-induced switching of AFM/HM structures. Thus, we estimate the range of *D* for various magnitudes of K_U, A_1 and A_2 using the following analytical relations as [S14]

$$D = \frac{16|K_U|\delta^2}{\pi\lambda} E\left(\frac{1}{\sqrt{C}}\right) K\left(\frac{1}{\sqrt{C}}\right) \quad (1)$$

where δ is the antiferromagnetic DW width, A_1 (> 0) corresponds to the inhomogeneous component of intra sublattice exchange constant, A_2 (< 0) is the inhomogeneous component of the inter-sublattice exchange constant, and K_U is the anisotropy constant, and λ corresponds to antiferromagnetic domain size. $E\left(\frac{1}{\sqrt{C}}\right)$ and $K\left(\frac{1}{\sqrt{C}}\right)$ are first and second-order complete elliptic integrals, where *C* is an integration constant. Using $\lambda \approx 100$ nm, from X-ray microscopy measurements (Fig. 4(l) of the main manuscript) and using the values of K_U, A_1, and A_2 from previous reports [S14-S17], we obtain the variation of *D* versus *C* (Figure S7). The range of *C* is constrained ($0 < C \leq 1$) within the two divergent limits of the elliptic integrals. As stated in the main manuscript, this estimate of *D* is close to a critical DMI constant (D_C), calculated with typical parameters reported for Mn-based metallic AFMs.

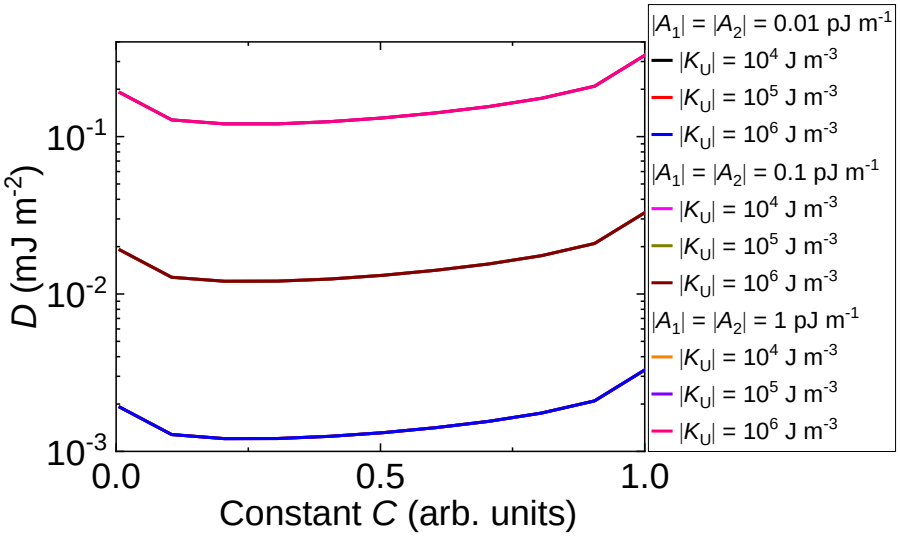

Figure S7: Estimation of DMI constant (*D*) versus integration constant (*C*), using the analytical formula. The range of C ($0 < C \leq 1$) is constrained within this limit owing to the diverging values of *D* for C =0, and C >1, respectively.

S8. Estimation of critical Dzyaloshinskii-Moriya constant (D_C) for multi-domain antiferromagnetic ground state in AFM/HM structures

For ferromagnet/HM multilayer systems, the presence of broken inversion symmetry results in interfacial chiral interactions (*e.g.,* DMI) which renders the stabilization of chiral spin textures (chiral Néel DWs or skyrmions) and shown to play an important role concerning SOT-induced magnetization switching. Owing to the ubiquitous presence of broken inversion symmetry, understanding and clarification of the role of DMI in AFM/HM structures are extremely important. Recent analytical and micromagnetic calculations have shown that the presence of DMI can stabilize a multi-domain inhomogeneous ground state in AFMs with easy-plane anisotropy component when the interfacial DMI constant (D) is comparable or larger than a critical value (D_C) [S14, S15]. This critical value of D_C is given by

$$D_C = \frac{2}{\pi}\sqrt{2(2A_1 - A_2)|K_U|} \quad (2)$$

where, A_1 (> 0) corresponds to the inhomogeneous component of intra sublattice exchange constant, A_2 (< 0) is the inhomogeneous component of inter-lattice exchange constant, and K_U is the anisotropy constant. Table T1 shows the estimate of D_C for A_1, A_2, and K_U within the range of typical values characteristic to Mn-based metallic AFMs. Interestingly, the estimated values of D_C are comparable to an estimation of D for PtMn/Pt structures. Note that D_C is also comparable to that for Pt/FM interfaces [S18]. Our results show a crucial role played by chiral interactions towards understanding of current-induced switching in AFM/HM structures.

A_1 (pJ m^{-1})	A_{12} (pJ m^{-1})	K_U (J m^{-3})	D_C (mJ m^{-2})	A_1 (pJ m^{-1})	A_{12} (pJ m^{-1})	D_C (mJ m^{-2})
0.01	-0.01	1×10^4	0.01	0.1	-0.1	0.05
0.01	-0.01	1×10^5	0.05	0.1	-0.1	0.15
0.01	-0.01	1×10^6	0.15	0.1	-0.1	0.49
1	-1	1×10^4	0.15	10	-10	0.49
1	-1	1×10^5	0.49	10	-10	1.56
1	-1	1×10^6	1.56	10	-10	4.93

Table T1: Estimate of critical Dzyaloshinskii-Moriya constant (D_C) for various magnitudes of anisotropy constant (K_U) and inhomogeneous component of intra sub lattice (A_1) and inter sublattice (A_2) exchange constants.

S9. Estimation of antiferromagnetic domain wall (DW) width

The static DW width for a two sublattice collinear AFM can be analytically expressed as [S14, S15]

$$\delta = \sqrt{\frac{2A_1 - A_2}{2|K_U|}} \tag{3}$$

where, A_1 (> 0) corresponds to the inhomogeneous component of intra sublattice exchange constant, A_2 (< 0) is the inhomogeneous component of inter-lattice exchange constant, and K_U is the anisotropy constant. Note that the analytical expression for δ is dependent only on the inhomogeneous components of exchange and magnitude of anisotropy constants, while is independent of the homogeneous component of exchange and the nature of the magnetic anisotropy (uniaxial or easy plane). Figures S8(a)-(c) shows the variation of δ versus A_1, A_2, and K_U, where the range of the variable parameters were chosen as in previous studies [S14-S17]. The obtained values of δ are smaller than the crystallite size ~ 10 nm (from X-ray diffraction), and the switchable antiferromagnetic domain size of ~ 100-200 nm (from XMLD measurements), indicating the feasibility of the antiferromagnetic spin texture-dominated reversal of antiferromagnetic Néel order parameter.

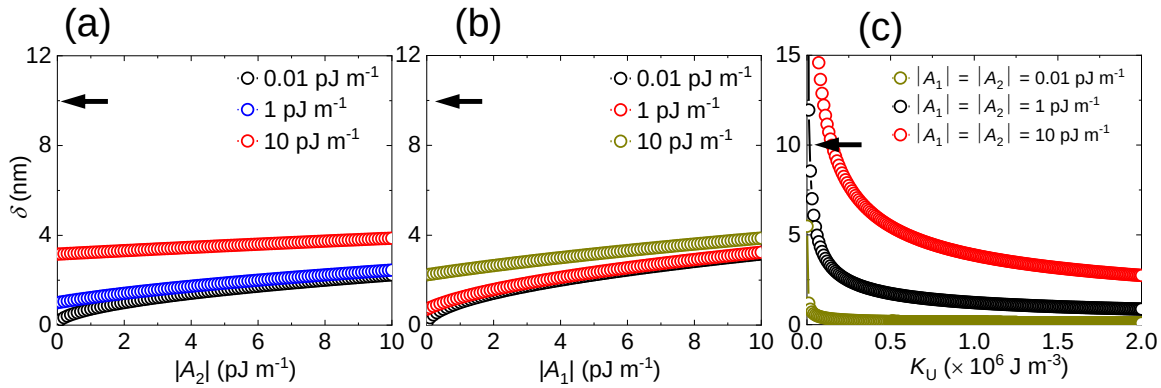

Figure S8: (a) AFM DW width (δ) versus $|A_2|$ for $|A_1|$ = 0.01, 1 and 10 pJ m^{-1} at K_U = 10^6 J m^{-3}. (b) variation of δ versus $|A_1|$ for $|A_2|$ = 0.01, 1 and 10 pJ m^{-1} at K_U = 10^6 J m^{-3}. (c) variation of δ versus K_U for different values of A_1 and A_2 spanning over four orders of magnitude. Black arrows in the figure indicate the mean crystallite size obtained from X-ray diffraction measurements.

S10. Calibration of temperature rise due to current pulse injection

The injection of current in PtMn/Pt and PtMn/Ru structures leads to an increase in temperature due to Joule heating. This temperature rise has been shown to result in significant effects on the antiferromagnetic Neel vector in other systems [S10, S11]. Thus, it is imperative to quantify the temperature rise in our PtMn/Pt and PtMn/Ru structures. The temperature rise is calibrated by measuring resistance of PtMn/Pt and PtMn/Ru for various applied dc current and converting the change of resistance into the change in temperature. Figure S9(a), (c) shows that the resistivity of the device increases with temperature, as expected for metallic systems. The temperature coefficient of the resistance is obtained from a fit of the temperature dependence of the resistivity measured between 50 and 300 K. The resistivity of the device increases as a function of current density in the PtMn layer J_{PtMn}. The obtained dependence can be fitted with a quadratic function CJ^2 (not shown), from which the coefficient (C) of resistivity as a function of J is obtained. From these results, the temperature rise is calculated, which is shown as a function of J_{PtMn} in Fig. S9(b). Owing to the larger current flow through the PtMn layer in PtMn(t_{PtMn})/Ru as compared to PtMn(t_{PtMn})/Pt structures, a larger temperature rise in PtMn/Ru structure occurs. The maximum temperature rise in PtMn/Ru at the highest applied current density is larger by more than a factor of 2 compared to PtMn/Pt. These results evidence the non-negligible role played by the temperature rise with the injection of current in PtMn/Ru structures. We believe that the gradual increase of R_{Hall} in PtMn/Ru is associated with the significant temperature rise in these structures, which may lead to electromigration, metastable fragmented domain states [S19], as well as to thermoelectric effects in addition to thermally-assisted Néel vector switching, re-orientation [S11] or nucleation and propagation of domain walls in the structure [S8, S14, S15].

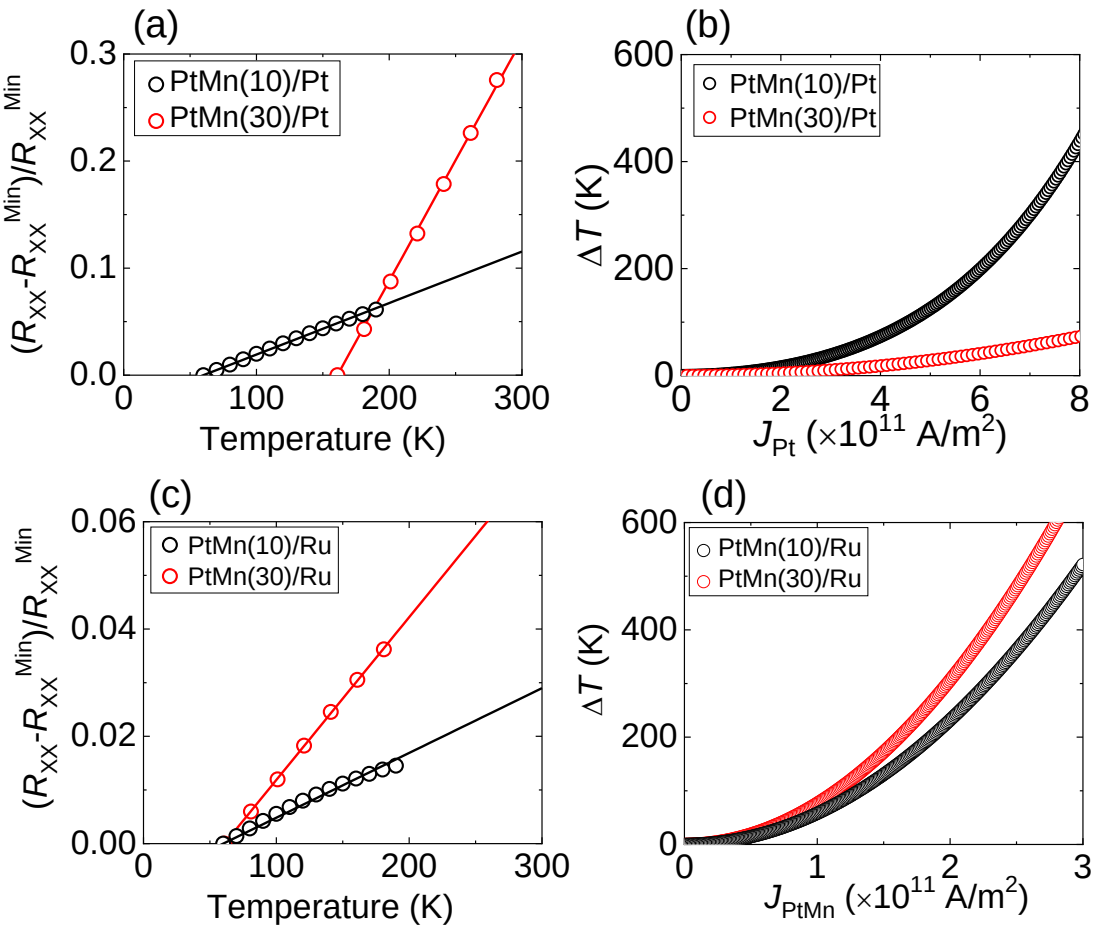

Figure S9: (a) Change in the longitudinal resistance (R_{XX}) of PtMn(10)/Pt and PtMn(30)/Pt structure as a function of temperature. (b) Calculated rise in temperature of the structures versus current density in the Pt (J_{Pt}) layer for PtMn/Pt structures. (c) Change in R_{XX} as a function of temperature for PtMn(10)/Ru and PtMn(30)/Ru structures. (d) Calculated rise in temperature of the structures versus J_{PtMn}.

S11. Optical micrograph of PtMn/Ru structures after current pulse application

To get a qualitative idea concerning the possibility of electrical stress, we take the optical micrograph of a PtMn(10)/Ru device utilized for current-induced switching measurements. The current-induced switching measurements for a similar device from the same wafer are shown in the main text (Fig. 2(b)). We observe darkened regions in the write current paths, while the central cross region remains relatively unaffected (Fig. S10). No significant changes were observed in the read current path. On the contrary, we donot observe any similar changes in PtMn(10)/Pt structures. These changes are indicative of heavy electrical stress owing to the significant current densities in PtMn/Ru structures.

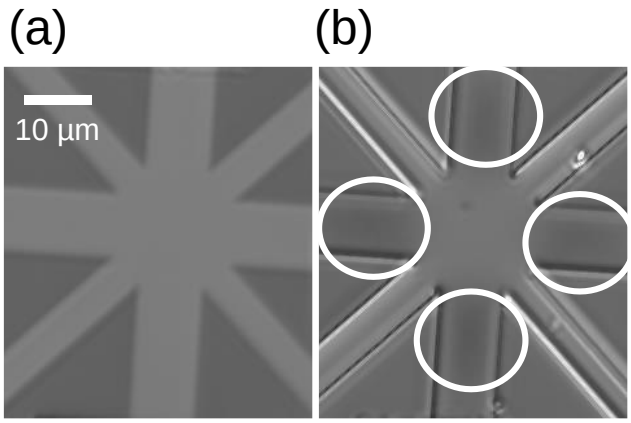

Figure S10: Optical micrograph of PtMn(10)/Ru structure (a) before electrical measurement, and (b) after electrical measurements. The white circled regions in (b) highlights the darkened areas in the device.

References

[S1] W. Mahler, Z. Metallkd. **46**, 282 (1955).
[S2] Ladwig, P. F. *et al.*, Paramagnetic to antiferromagnetic phase transformation in sputter deposited Pt-Mn thin films, J. Appl. Phys. **94**, 979 (2003).
[S3] Peng, T. Y. *et al.*, Study of annealing and exchange bias effects in PtMn based magnetic tunnel junctions, Phys. Stat. Sol. (c) **1**, 3628 (2004).
[S4] Chiang, C. C., Huang, S. Y., Qu, D., Wu, P. H & Chien, C. L., Absence of Evidence of Electrical Switching of the Antiferromagnetic Néel vector, Phys. Rev. Lett. **123**, 227203 (2019).
[S5] Wadley, P. *et al.* Current-polarity-dependent manipulation of antiferromagnetic domains. Nature. Nanotech. **13**, 362 (2018).
[S6] Taylor, J. *et al.*, Magnetic and electrical transport signatures of uncompensated moments in epitaxial thin films of the noncollinear antiferromagnet Mn_3Ir, Appl. Phys. Lett. **115**, 062403 (2019).
[S7] Sakuma A., First-Principles Study of the Non-collinear Magnetic Structures of Disordered Alloys, Journ. Phys. Soc. Jpn. **69**, 3072 (2000).
[S8] Baldarati, L. *et al.* Mechanism of Néel order switching in antiferromagnetic thin films revealed by magnetotransport and imaging techniques, Phys. Rev. Lett. **123**, 177201 (2019).
[S9] Wadley, P. *et al.* Electrical switching of an antiferromagnet. *Science* **351**, 587-590 (2016).
[S10] Bodnar, S. Y. *et al.* Writing and reading of antiferromagnetic Mn_2Au by Néel spin-orbit torques and large anisotropic magnetoresistance. *Nature Commun.* **9**, 348 (2018).
[S11] Meinert, M., Graulich, D. & Mallata-Wagner, T. Electrical Switching of Antiferromagnetic Mn_2Au and the Role of Thermal Activation. *Phys. Rev. Appl.* **9**, 064040 (2018).
[S12] Chen, X. Z. *et al.* Antidamping-Torque-Induced Switching in Biaxial Antiferromagnetic Insulators. *Phys. Rev. Lett.* **120**, 207204 (2018).
[S13] Moriyama, T., Oda, K., Ohkochi, T., Kimata, M. & Ono, T. Spin torque control of antiferromagnetic moments in NiO. *Sci. Rep.* **8**, 14167 (2018).
[S14] Tomasello, R. *et al*. Domain periodicity in an easy-plane antiferromagnet with Dzyaloshinskii-Moriya interaction, arXiv:2004.01944 (2020).
[S15] Sanchez-Tejerina L., Puliafito V., Amiri P. K., Carpentieri M. & Finocchio G., Dynamics of domain-wall motion driven by spin-orbit torques in antiferromagnets, Phys. Rev. B. **101**, 014433 (2020).
[S16] Umetsu, R. Y., Sakuma, A. & Fukamichi, K. Magnetic anisotropy energy of antiferromagnetic L10-type equiatomic Mn alloys. Appl. Phys. Lett. **89**, 052504 (2006).
[S17] Xu, Y., Wang, S. & Xia, K. Spin-Transfer Torques in Antiferromagnetic Metals from First Principles, Phys. Rev. Lett. **100**, 226602 (2008).
[S18] DuttaGupta, S. *et al*. Spin-orbit torques and Dzyaloshinskii-Moriya interaction in PtMn/[Co/Ni] heterostructures, Appl. Phys. Lett. **11**1, 182412 (2017).
[S19] Wörnle, M. S. *et al.* Current-induced fragmentation of antiferromagnetic domains. arXiv:1912.05287v1 (2019).